

MISCLASSIFIED TYPE 1 AGNs IN THE LOCAL UNIVERSE

JONG-HAK WOO¹, JI-GANG KIM^{1,2}, DAESEONG PARK³, HYUN-JIN BAE⁴, JAE-HYUK KIM², SEUNG-EON LEE²,
SANG CHUL KIM⁵, AND HONG-JIN KWON²

¹Astronomy Program, Department of Physics and Astronomy, Seoul National University, Seoul 151-742, Korea;
woo@astro.snu.ac.kr

²R&E Program, Gyeonggi Science High School for the Gifted, 68-23 Songjuk, Jangan, Suwon 440-800, Korea

³Department of Physics and Astronomy, University of California Irvine, CA, USA

⁴Department of Astronomy and Center for Galaxy Evolution Research, Yonsei University, Seoul 120-749, Korea

⁵Korea Astronomy and Space Science Institute, Daejeon 305-348, Korea

Received —; accepted —

Abstract: We search for misclassified type 1 AGNs among type 2 AGNs identified with emission line flux ratios, and investigate the properties of the sample. Using 4113 local type 2 AGNs at $0.02 < z < 0.05$ selected from Sloan Digital Sky Survey Data Release 7, we detected a broad component of the $H\alpha$ line with a Full-Width at Half-Maximum (FWHM) ranging from 1700 to 19090 km s^{-1} for 142 objects, based on the spectral decomposition and visual inspection. The fraction of the misclassified type 1 AGNs among type 2 AGN sample is $\sim 3.5\%$, implying that a large number of missing type 1 AGN population may exist. The misclassified type 1 AGNs have relatively low luminosity with a mean broad $H\alpha$ luminosity, $\log L_{H\alpha} = 40.50 \pm 0.35 \text{ erg s}^{-1}$, while black hole mass of the sample is comparable to that of the local black hole population, with a mean black hole mass, $\log M_{\text{BH}} = 6.94 \pm 0.51 M_{\odot}$. The mean Eddington ratio of the sample is $\log L_{\text{bol}}/L_{\text{Edd}} = -2.00 \pm 0.40$, indicating that black hole activity is relatively weak, hence, AGN continuum is too weak to change the host galaxy color. We find that the OIII lines show significant velocity offsets, presumably due to outflows in the narrow-line region, while the velocity offset of the narrow component of the $H\alpha$ line is not prominent, consistent with the ionized gas kinematics of general type 1 AGN population.

Key words: galaxies: active — galaxies: nuclei — galaxies: Seyfert: $H\alpha$ emission line

1. INTRODUCTION

Large-area surveys performed in various wavelengths, i.e., X-ray, optical, near-infrared, and mid-infrared, provide a large sample of active galactic nuclei (AGNs), enabling various statistical studies of actively mass accreting supermassive black holes. In particular, by providing the rest-frame optical and UV spectroscopic properties of more than 100 000 AGNs over a large redshift range, the Sloan Digital Sky Survey (SDSS) has dramatically changed our understanding of AGN population (e.g., Abazajian et al. 2009), including the local black hole activity (see Heckman & Best 2014), AGN luminosity and Eddington ratio functions from low- to high-redshift (e.g., Kelly & Shen 2013), and the connection of black hole activity to star formation (e.g., Netzer 2009).

However, all surveys have their selection functions, hence, it is challenging to avoid selection biases in providing a complete sample of AGNs. In the case of the SDSS, the color-color diagram based on the imaging survey has been used for selecting potential AGN candidates as spectroscopic follow-up targets. Thus, obscured AGNs, i.e., red AGNs (e.g., Glikman et al. 2007, 2013) and X-ray-bright-optically-normal AGNs (e.g., Hornschemeier et al. 2005), can be easily missed from the survey.

In the optical spectroscopic studies, type 1 and type 2 AGNs are often classified based on the presence or absence of broad-emission lines, which are usually defined having a FWHM larger than 1000 km s^{-1} , as initially recognized among nearby Seyfert galaxies (e.g., Seyfert 1943). However, if the broad component of the Balmer lines is relatively weak and/or the narrow component is dominant, then it is likely that type 1 AGNs can be misclassified as type 2 AGNs. In addition, if the AGN continuum is relatively weak compared to the stellar continuum, then these objects are likely to be classified as galaxies rather than AGNs in the color-color diagram.

A number of statistical studies have been performed using the SDSS galaxy catalogues, e.g., the MPA-JHU value-added catalog,¹ and the KIAS value-added galaxy catalog (Choi et al. 2010), which contain the flux-limited local galaxy sample out to $z \sim 0.2$, to investigate the properties of type 2 AGN populations identified through the emission line flux ratios (Baldwin et al. 1981; Kewley et al. 2006). It has been noticed that some type 2 AGNs show a relatively broad component in the $H\alpha$ line, while a broad component is often missing in the $H\beta$ line, presumably due to its weak flux compared to the stellar continuum, suggesting that at least some fraction of type 2 AGNs identi-

CORRESPONDING AUTHOR: J.-H. Woo

¹<http://www.mpa-garching.mpg.de/SDSS/>

fied through their emission line ratios could be genuine type 1 AGNs. A systematic search for these misclassified type 1 AGNs is yet to be performed (see, e.g., Oh et al. 2011; Bae & Woo 2014). These misclassified AGNs are interesting targets for further study since they are likely to be low luminosity AGNs since their AGN continuum is relatively weak. At the same time, their host galaxy properties can be easily studied while the mass of the central black hole can be estimated from the broad component of $H\alpha$ using various single-epoch mass estimators (e.g., Woo & Urry 2002; Park et al. 2012; Bentz et al. 2013).

In this paper, we search for misclassified type 1 AGNs using a large sample of local type 2 AGNs selected from SDSS DR7, by carefully examining the presence of the broad component of the $H\alpha$ line. Based on the newly found type 1 AGNs, we investigate the properties of black hole activity and the kinematics of the ionized gas. Sample selection and the procedure for identifying type 1 AGNs are described in Sections 2 and 3, respectively. In Section 4, we present the properties of the newly found 142 type 1 AGNs and their gas properties. Discussion and conclusions are presented in Section 5. Throughout the paper, we used the cosmological constants of $H_0 = 70 \text{ km s}^{-1} \text{ Mpc}^{-1}$, $\Omega_m = 0.3$, and $\Omega_\Lambda = 0.7$.

2. SAMPLE SELECTION

To select type 2 AGNs in the local universe, we utilized the MPA-JHU catalog, which contains 927 552 galaxies from the SDSS DR 7 and their derived properties. We selected low-redshift galaxies (i.e., $0.02 < z < 0.05$) and excluded galaxies with low stellar velocity dispersion (i.e., below the SDSS instrumental resolution, $\sigma < 70 \text{ km s}^{-1}$) in order to utilize the available stellar velocity dispersion measurements in comparing with the gas kinematics. Among these local galaxies, we selected emission-line objects with signal-to-noise ratio $S/N \geq 3$ for $H\alpha$, $H\beta$, $O\text{I}$, and $O\text{III}$, which were used to classify AGNs in the emission line flux ratio diagram (Baldwin et al. 1981). By using the demarcation line for AGNs and star-forming galaxies, $0.73/[\log O\text{I}/H\alpha + 0.59] + 1.33 < \log O\text{III}/H\beta$ or $\log O\text{I}/H\alpha > -0.59$ (Kewley et al. 2006), we selected 4 113 objects as the type 2 AGN sample.

3. ANALYSIS

3.1. Spectral Decomposition

In studying type 2 AGNs, it is of importance to decompose AGN emission lines from the host galaxy stellar continuum in order to properly measure the flux and width of each AGN emission line. For relatively low luminosity AGNs, the line strength of stellar absorption lines is significantly large, hence the precise measurements of AGN emission line flux requires spectral decomposition of the stellar component, for example, using stellar population models or stellar spectral templates (e.g., Park et al. 2012). In addition, for measuring the kinematics of the ionized gas, it is

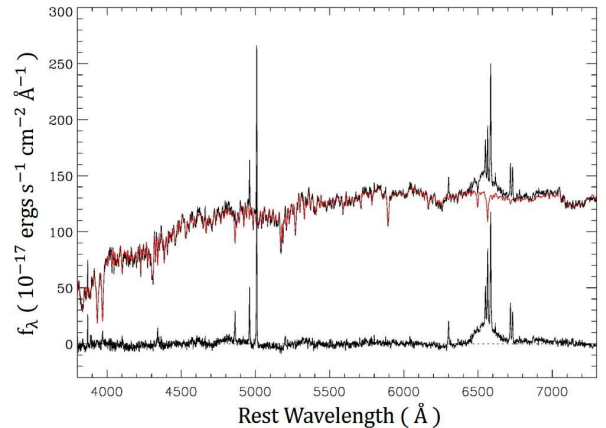


Figure 1. Example of the spectral decomposition for SDSS J140543.16+251352.9. The SDSS spectrum (black line) is modeled with a stellar population model (red line). The residual spectrum at the bottom represents a pure AGN emission line spectrum.

necessary to measure the systemic velocity of the target galaxy based on the stellar absorption lines. In this study, we used the penalized pixel-fitting (pPXF) method (Cappellari & Emsellem 2004) to obtain the best fit stellar continuum model, which is based on the 235 simple stellar population models (i.e., 5 different metallicities \times 47 different ages) from the MILES library. First, we de-redshifted all spectra using the redshift value from SDSS. After fitting with the stellar continuum model, we refined the redshift (hence, the systemic velocity) of each object before the emission line fitting procedure. Then, the best-fit continuum model was subtracted from the SDSS spectra, leaving the pure AGN emission-line spectra. This approach is similar to a number of previous studies on the AGN emission and stellar absorption lines (e.g., Woo et al. 2010; Park et al. 2012; Woo et al. 2013). We present an example of the spectral decomposition in Figure 1.

3.2. Emission Line Fitting

We examined the SDSS spectra and continuum-subtracted spectra of all 4,113 objects in the type 2 AGN sample, in order to determine whether a broad component is present in the $H\alpha$ line. In this process, we identified a sample of potential type 1 AGN candidates showing the broad $H\alpha$ component, based on the visual inspection. Then, we carefully examined the $H\alpha$ region in the rest-frame 6300–6900Å, by decomposing the broad and narrow components of $H\alpha$, and $N\text{II}$ lines simultaneously. If the stellar continuum was poorly subtracted from the SDSS spectra due to the low S/N ratio, a straight line was adopted to represent the continuum.

Using the MPFIT routine (Markwardt 2009), we modeled each narrow emission line in the $H\alpha$ region, namely, $H\alpha$ $\lambda\lambda 6563$, $N\text{II}$ $\lambda\lambda 6548, 6583$ doublet, and $S\text{II}$ $\lambda\lambda 6716, 6731$ doublet with a single Gaussian component. In addition, we added a Gaussian component

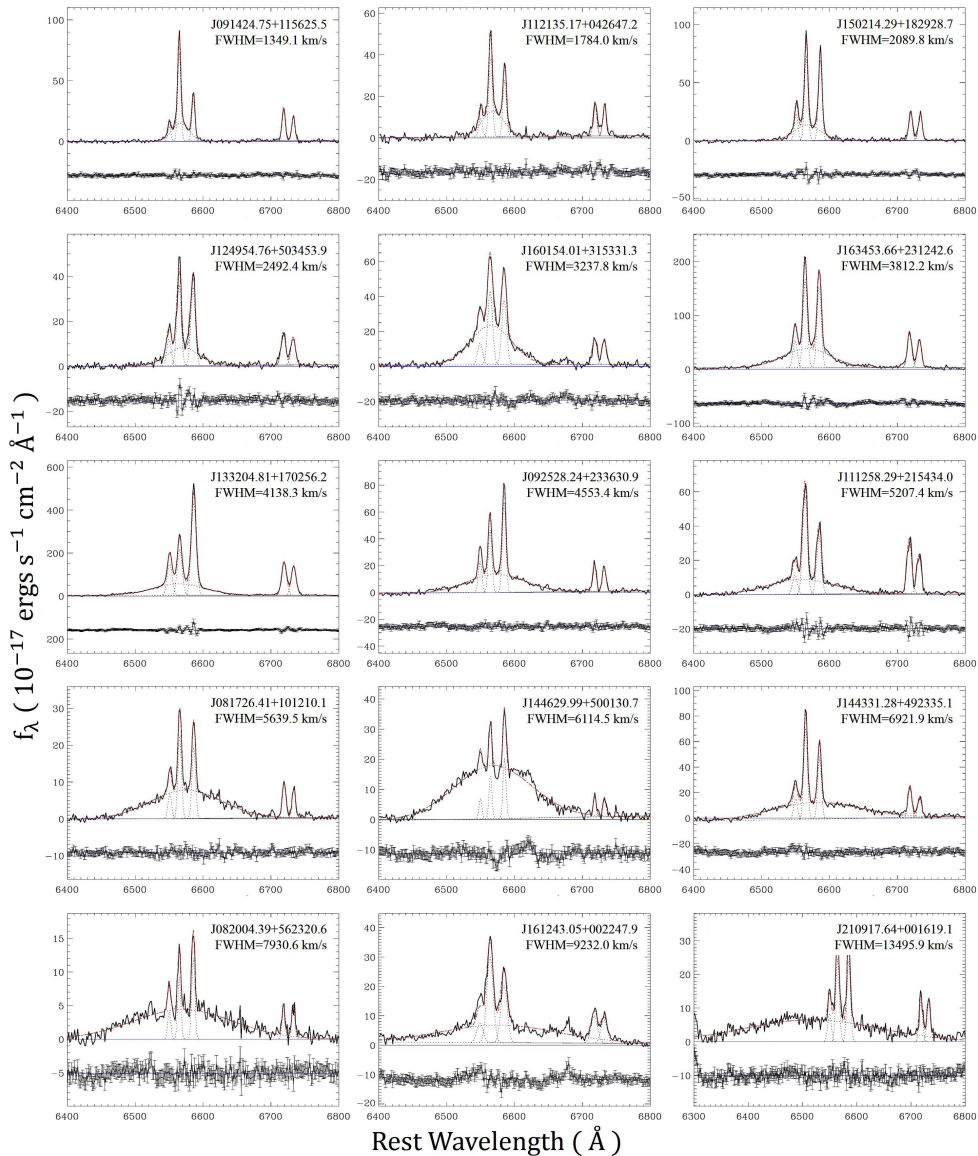


Figure 2. Examples of the best-fit emission line models in the $H\alpha$ region for 15 objects, are presented in order of increasing FWHM of the broad $H\alpha$ component. Continuum-subtracted spectra (black lines) are plotted together with the best-fit models (red lines), which are composed of narrow lines (N II, $H\alpha$, and S II) and a broad $H\alpha$ component. At the bottom of each panel the residual is presented (black lines). The object name and the FWHM of the broad $H\alpha$ component are given in each panel.

with a $\text{FWHM} > 1000 \text{ km s}^{-1}$, to represent the broad component of $H\alpha$. The centers of each Gaussian components for narrow emission lines were fixed relative to each other at their laboratory separations, while the center of the broad $H\alpha$ component was set to vary in the fitting process. In the case of the line width, we used the same line dispersion value for all narrow emission lines, but for the broad $H\alpha$ component, we used a free parameter. The line flux ratio of [N II] $\lambda 6583$ and [N II] $\lambda 6548$ is fixed at the theoretical value of 2.96.

Note that a broad residual from the incorrect subtraction of stellar continuum or the combination of the narrow $H\alpha$ and N II line wings could be misinterpreted as a broad-line component. Thus, a careful examina-

tion is required to avoid false detection of a broad $H\alpha$ component. For each object, we carefully examined and compared the raw spectrum and the best-fit model, and conservatively classified the target as type 1 AGNs only if the broad $H\alpha$ component is clearly needed for the fit. In particular, when the broad $H\alpha$ is relatively narrow (i.e., $\text{FWHM} < \sim 2000 \text{ km s}^{-1}$), hence we do not see the wing of the broad $H\alpha$ blueward and redward of N II in the continuum-subtracted spectra, we removed the target from the list of the type 1 AGN candidates although the best-fit model includes a broad $H\alpha$ component. Thus, in our conservative classification it is possible that we may miss relatively narrow broad-line objects (e.g., narrow-line Seyfert 1 galaxies). In this

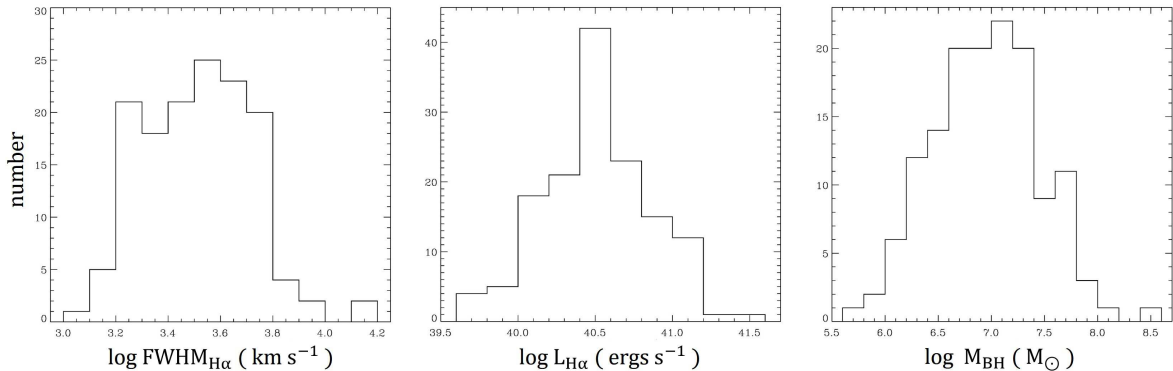


Figure 3. Distribution of the measured $\text{FWHM}_{H\alpha}$ (left), $\log L_{H\alpha}$ (center), $\log M_{\text{BH}}$ (right) for 142 misclassified type 1 AGNs.

process, we identified 142 AGNs, which clearly showed a broad $H\alpha$ component. Figure 2 presents examples of the emission line fit in the $H\alpha$ region for 15 AGNs in increasing magnitude of the FWHM of the broad $H\alpha$ component.

We measured the line flux and line dispersion of each narrow emission line and the broad $H\alpha$ line from the best-fit model. We used the luminosity distance using the redshift information in the header of the fits file or the measured redshift from the stellar absorption lines. These two redshifts showed negligible difference in luminosity distance. Figure 3 presents the distributions of the widths and luminosities of the broad $H\alpha$ component (see Section 4.1 for details).

We also fit the O III line at 5007\AA , to measure the velocity center and the velocity dispersion. Since the majority of the AGNs in the sample show a broad wing component in the O III line profile, we used a double Gaussian model to fit the line profile. Then, we measured the flux centroid velocity and velocity dispersion of the best-fit double-Gaussian model.

3.3. Black Hole Mass and Eddington ratio

Dynamical black hole mass estimation based on the spatially resolved kinematics is limited to nearby galaxies due to the limited spatial resolution (Kormendy & Ho 2013). For broad-line AGNs, black hole mass (M_{BH}) can be measured with the reverberation mapping method based on the virial assumption of the gas in the broad-line region (BLR) (Blandford & McKee 1982). Under the virial relation, black hole mass is expressed as $M_{\text{BH}} = f V^2 R_{\text{BLR}}/G$, where V is the characteristic velocity scale of the broad-line gas, typically measured from the line dispersion of the Balmer lines, f is the virial coefficient, which depends on the morphology, orientation, and the kinematics of the BLR, R_{BLR} is the size of the BLR measured from the reverberation mapping campaign, and G is the gravitational constant.

Adopting the BLR size – luminosity relation from the recent calibration by Bentz et al. (2013),

$$R_{\text{BLR}} = 10^{1.527} \left[\frac{\lambda L_{5100}}{10^{44} \text{ erg s}^{-1}} \right]^{0.533} \text{ light days} \quad (1)$$

the virial relation can be written as follows:

$$M_{\text{BH}} = f \times 10^{6.817} \left[\frac{V}{10^3 \text{ km s}^{-1}} \right]^2 \times \left[\frac{\lambda L_{5100}}{10^{44} \text{ erg s}^{-1}} \right]^{0.533} M_{\odot}. \quad (2)$$

For the misclassified AGNs, we used the line width and luminosity of the broad $H\alpha$ for estimating black hole masses. Adopting the calibration between the widths of $H\beta$ and $H\alpha$ (i.e., $\text{FWHM}_{H\beta}$ – $\text{FWHM}_{H\alpha}$ relation), and the relation between the AGN continuum luminosity and the $H\alpha$ line luminosity (i.e., L_{5100} – $L_{H\alpha}$ relation) from Greene & Ho (2005),

$$\text{FWHM}_{H\beta} = 1.07 \times 10^3 \left[\frac{\text{FWHM}_{H\alpha}}{10^3 \text{ km s}^{-1}} \right]^{1.03} \text{ km s}^{-1}, \quad (3)$$

we can derive M_{BH} from our measurements based on the spectroscopic decomposition in the $H\alpha$ region. With the line dispersion ($\sigma_{H\alpha}$) and luminosity ($L_{H\alpha}$) of the broad component of $H\alpha$, the black hole mass can be estimated as follows:

$$M_{\text{BH}} = f \times 10^{6.565} \left[\frac{\sigma_{H\alpha}}{10^3 \text{ km s}^{-1}} \right]^{2.06} \times \left[\frac{L_{H\alpha}}{10^{42} \text{ erg s}^{-1}} \right]^{0.46} M_{\odot}. \quad (4)$$

For the virial factor we adopted $f = 5.9_{-1.5}^{+2.1}$, which is based on the recent calibration using the combined sample of the quiescent galaxies and reverberation-mapped AGNs (Woo et al. 2013). Note that the systematic uncertainty of the virial factor is 0.31 dex (see Woo et al. 2010) and that black hole mass can easily vary by a factor of 2–3, depending on the virial factor calibration (see Park et al. 2012). Thus, the quoted black hole mass should be treated with caution. In Table 1, we provide the virial product, instead of the black hole mass, which can be determined by multiplying the virial product with the virial factor.

The Eddington luminosity of each object was calculated with the equation $L_{\text{Edd}} = 1.25 \times 10^{38} M_{\text{BH}}$

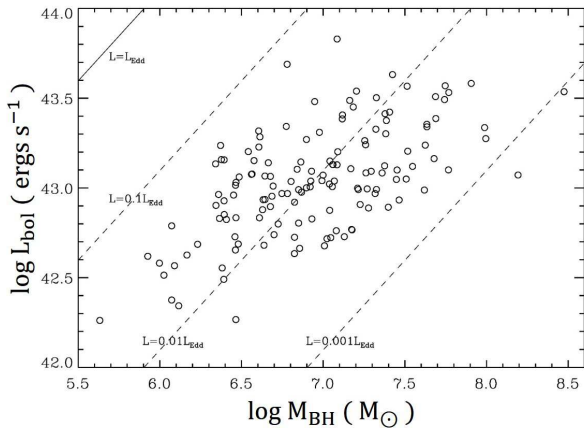


Figure 4. Bolometric luminosity vs. black hole mass for 142 misclassified type 1 AGNs. Dashed lines represent fixed Eddington ratios.

(erg s^{-1}) (Wyithe & Loeb 2002). We used the luminosity of the broad $H\alpha$ line as a proxy for the AGN bolometric luminosity Utilizing the relation between the luminosity of broad $H\alpha$ and the continuum luminosity at 5100\AA (Greene & Ho 2005), and the bolometric correction 9.26 for L_{5100} (Richards et al. 2006), we derived the bolometric luminosity as follows,

$$L_{bol} = 2.21 \times 10^{44} \left(\frac{L_{H\alpha}}{10^{42} \text{ erg s}^{-1}} \right)^{0.86} \text{ erg s}^{-1}. \quad (5)$$

4. RESULTS

4.1. Sample Properties

Out of the parent sample of 4113 type 2 AGNs in the local universe ($0.02 < z < 0.05$), we find a total of 142 misclassified type 1 AGNs based on the presence of the broad component of $H\alpha$ ($\text{FWHM} > 1000 \text{ km s}^{-1}$). The fraction of misclassified AGNs is $\sim 3.5\%$ of the parent sample. 25 objects have been previously referenced in the literature (see Greene & Ho 2004, 2007; Xiao et al. 2013; Reines et al. 2013), indicating a novel discovery of missing type 1 AGNs.

The distribution of the measured properties, i.e., the FWHM and luminosity of the broad $H\alpha$ component, and black hole mass, are presented in Figure 3. The newly identified type 1 AGNs have a large range of the broad $H\alpha$ FWHM velocities, ranging from 1700 to 19090 km s^{-1} . The mean line width of broad $H\alpha$ is $\log \text{FWHM}_{H\alpha} = 3.52 \pm 0.21$. In the case of the luminosity, all candidates are relatively low-luminosity AGNs with $H\alpha$ luminosity lower than $10^{42} \text{ erg s}^{-1}$. The mean broad $H\alpha$ luminosity is $\log L_{H\alpha} = 40.51 \pm 0.34$. The black hole mass of the sample ranges from $\sim 10^{5.5}$ to $\sim 10^{8.5} M_{\odot}$ with a mean $\log M_{BH}/M_{\odot} = 6.94 \pm 0.51$, while the mean Eddington ratio is $\log L_{bol}/L_{Edd} = -2.00 \pm 0.40$. Compared to the local supermassive black hole population, the misclassified AGNs have a similar black hole mass range with a peak at $\sim 10^7 M_{\odot}$

(Heckman & Best 2014), while the Eddington ratio of the sample is relatively lower than the one of high luminosity QSOs. Table 1 provides the list of 142 misclassified type 1 AGNs along with the measured physical parameters. Figure 4 presents the distribution of the misclassified type 1 AGNs in the $L_{bol} - M_{BH}$ plane. Overall, the distribution of the sample is similar to that of low luminosity type 1 AGNs (e.g., Woo & Urry 2002).

4.2. Comparison with MPA-JHU

In this section, we compare our new measurements of the $H\alpha$ line luminosity with that from the the MPA-JHU catalog as shown in Figure 5. Since the broad component of $H\alpha$ was included in our analysis, we expect that our measurements of the narrow $H\alpha$ line luminosity is reliable, while the MPA-JHU measurements are likely to be overestimated if the broad $H\alpha$ is not considered in the fitting process.

We find a clear trend that the narrow $H\alpha$ emission line flux measurements provided by the MPA-JHU catalog is larger than that of our measurement, particularly at the low luminosity regime. The overall overestimation of the narrow $H\alpha$ line flux can be interpreted as the contribution of the broad $H\alpha$, since the narrow and broad components were not decomposed, although the line flux can vary depending on how the continuum around the $H\alpha$ region was determined. The difference is less significant for AGNs with a strong narrow $H\alpha$ line, presumably due to the weaker contribution of the broad $H\alpha$ component. These results demonstrate that the line flux measurements of the narrow $H\alpha$ can be significantly uncertain when a broad component is present and that decomposing and subtracting a broad $H\alpha$ component from narrow lines (i.e., $H\alpha$ and $N\text{II}$) is necessary for misclassified type 1 AGNs.

4.3. Velocity offset of the emission lines

We investigate the kinematic properties of the ionized gas, by calculating the velocity offset of the $[\text{O III}]$ and the $H\alpha$ lines with respect to the systematic velocity, which is measured from stellar absorption lines. In the case of $H\alpha$, we use the narrow and broad components separately, since the physical scale of these two components is clearly different. In Figure 6, we present the distribution of the velocity offset for each line. For the $[\text{O III}]$ line, we used the flux centroid of the line profile as the velocity of the line if a double Gaussian model was used for the fit. The $[\text{O III}]$ line shows large velocity offsets ranging from ~ -350 to $\sim 100 \text{ km s}^{-1}$, with a mean -32 km s^{-1} and rms 67 km s^{-1} . In addition, the distribution of the $[\text{O III}]$ velocity offset is asymmetric, indicating that more than a half of the objects has blueshifted $[\text{O III}]$ with relatively large velocities. The detected velocity offset with respect to the systemic velocity can be interpreted as due to outflows in the narrow-line region, as various previous studies have used the $[\text{O III}]$ velocity offset as an outflow indicator (e.g., Boroson 2005; Komossa et al. 2008; Crenshaw et al. 2010; Bae & Woo 2014).

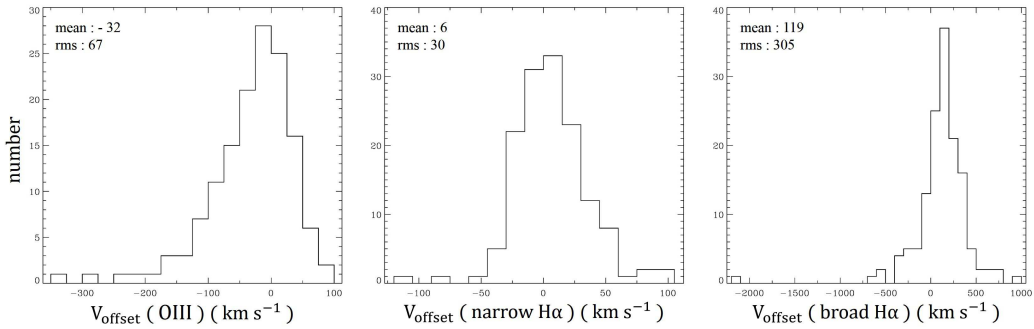


Figure 6. Distribution of the velocity offset with respect to the systemic velocity measured from stellar absorption lines. The O III line (left) presents on average a larger velocity offset than the narrow component of H α (center). The broad component of H α shows a significantly larger velocity offset than the narrow lines (right). In each panel, the mean and rms of the velocity offset is presented.

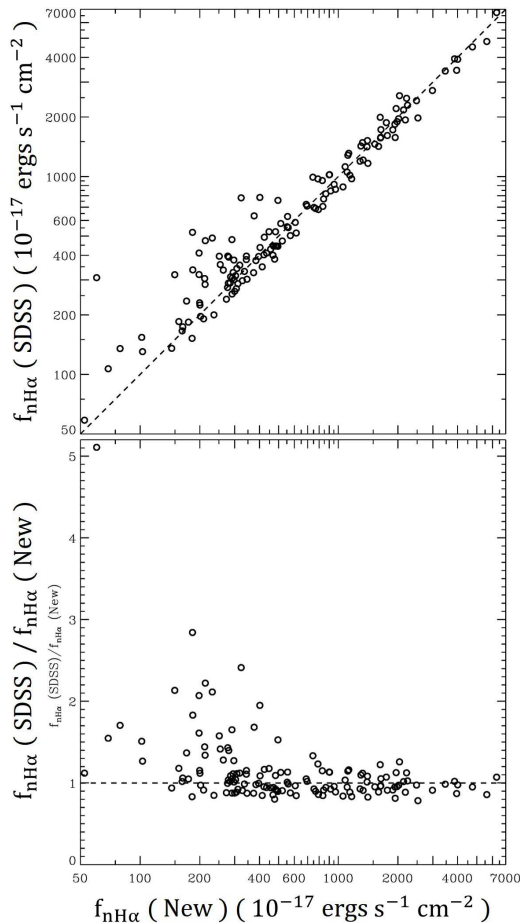


Figure 5. Comparison of the narrow H α flux measurements of 142 misclassified type 1 AGNs adopted from the MPA-JHU catalog and from this study.

In the case of the narrow H α component, most galaxies show relatively small velocity offsets with a mean 6 km s^{-1} and rms 30 km s^{-1} . Given the uncertainty of the emission line velocity, which is close to $10\text{--}20 \text{ km s}^{-1}$ as measured from simulated mock spectra based on

the SDSS spectra by Bae & Woo (2014), only a small fraction of the sample seems to show a significant H α velocity offset. These results of O III and H α velocity offsets are consistent with previous studies of type 2 AGNs (Komossa et al. 2008; Bae & Woo 2014).

In contrast, we detected large velocity offsets in the broad component of H α , with a mean velocity 119 km s^{-1} and with a rms of 305 km s^{-1} , which is much larger than that of narrow emission lines (H α and O III). The nature of the velocity offset of the broad line is not clear without spatially resolved measurements. We speculate that it may be due to the orbital motion of the black hole and accompanied BLR gas or the inflow/outflow motion of the gas in the BLR. More detailed studies are required to identify the nature of the velocity offset of broad emission lines.

4.4. Kinematics of the ionized gas

In Figure 7 we present the velocity dispersion of the ionized gas. For O III we calculated the second moment of the total line profile as the velocity dispersion when we used a double Gaussian model for the fit. In the case of N II and S II, we used the line dispersion of the best-fit Gaussian model. Since we used the same Gaussian model for N II and S II, we only present the velocity dispersion of N II.

Compared to the N II lines, the velocity dispersion of O III is much larger, by a factor 1.8 in average. The larger O III velocity dispersion is expected from the presence of a wing component in the line profile. However, once we remove the wing component and measure the velocity dispersion from the narrower core component from the best-fit double Gaussian models (bottom panel in Figure 7), the velocity dispersions of N II and O III become consistent albeit with significant scatter ($\sim 30\%$). The mean difference of the velocity dispersion between N II and the O III core component is only $\sim 1\%$, confirming that the core component of O III and low-ionization lines (i.e., N II and S II) have similar kinematics, presumably governed by the gravitational potential of the galaxy bulge (see also Komossa et al. 2008).

In Figure 8 we directly compare the velocity disper-

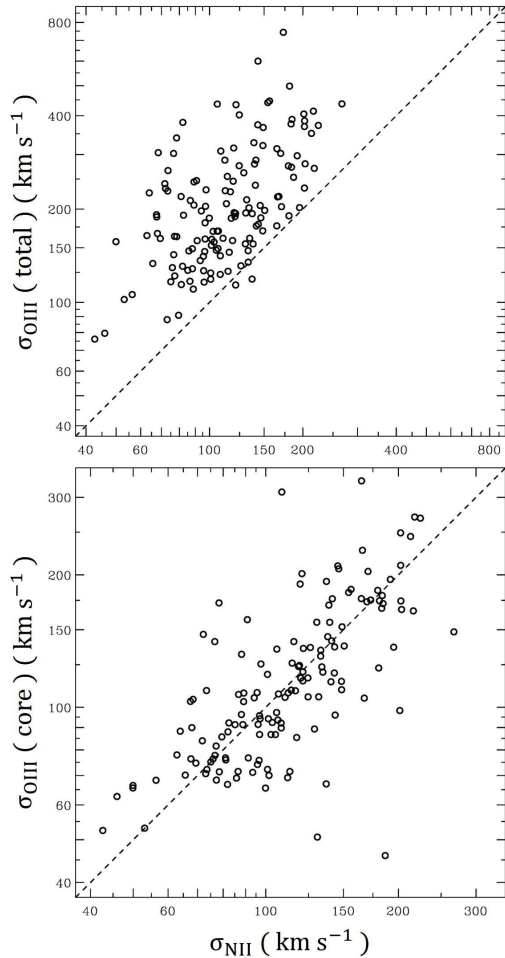


Figure 7. Comparison of the line dispersion of N II with that of total (top) and core component of [O III] (bottom). While the O III line is clearly broader than N II due to the strong wing component, the core component of O III shows consistent line dispersion compared to N II.

sion of N II and the core component of O III with stellar velocity dispersion. The velocity dispersion of N II is on average smaller than the stellar velocity dispersion by 14%, while the scatter is $\sim 29\%$. In the case of the core component of O III (bottom panel in Figure 8), the velocity dispersion is also smaller than the stellar velocity dispersion by 13%, however the scatter is considerably larger ($\sim 43\%$). These results suggest that the velocity dispersions of narrow emission lines are on average consistent with stellar velocity dispersions, confirming the results of previous studies (e.g., Nelson & Whittle 1995). Thus, the width of N II (or O III core component) may be used as a proxy for stellar velocity dispersion. However, if the velocity dispersions of the narrow-emission lines are used instead of the directly measured stellar velocity dispersions, significantly larger uncertainty would be introduced due to the large scatter shown in Figure 8.

The large scatter between emission and absorption lines can be attributed to the contribution from outflow

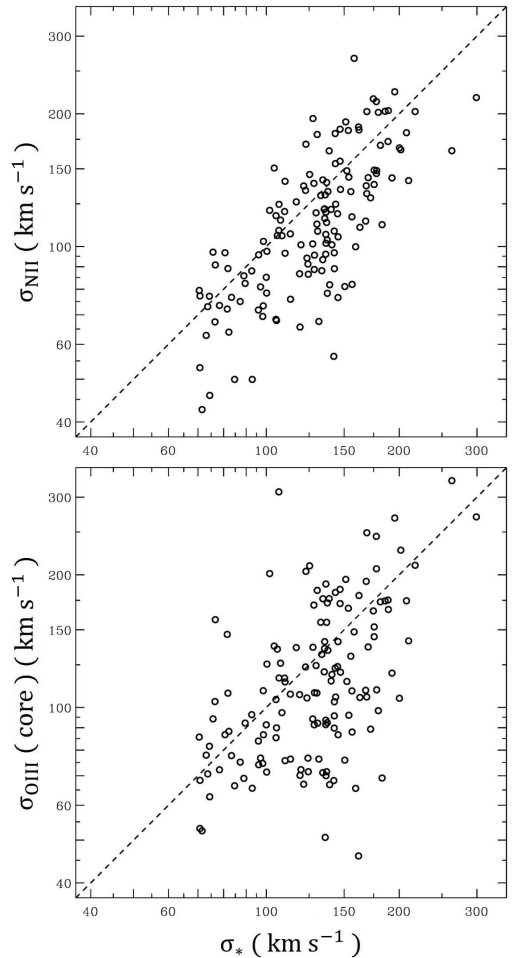


Figure 8. Comparison of the stellar velocity dispersion with the velocity dispersions of N II (top) and the core component of [O III] (bottom).

or inflow motion of the gas in the NLR, which seems to preferentially affect the O III-emitting gas. In addition, we note that the measured stellar velocity dispersion from the SDSS spectra, which were extracted with a $3''$ aperture, can suffer from rotational broadening in the stellar absorption lines, depending on the orientation of the stellar disk and the relative strength of the rotation and random velocities as demonstrated by the spatially resolved measurements (Kang et al. 2013; Woo et al. 2013) and the simulated results with various line-of-sight measurement (Bellovary et al. 2014). The larger stellar velocity dispersion relative to the velocity dispersion of N II, by 0.06 dex (14%), may indicate an overestimate of the stellar velocity dispersion due to the rotation/inclination effect.

5. DISCUSSION AND CONCLUSIONS

We presented a sample of 142 misclassified type 1 AGNs identified out of a parent sample of 4113 type 2 AGNs at $0.02 < z < 0.05$, selected from the SDSS DR 7 based on the emission-line flux ratios. The fraction of the misclassified type 1 AGNs among type 2 AGNs is $\sim 3.5\%$;

Table 1
Physical parameters of 142 missing type 1 AGNs

AGN (1)	z (2)	$\text{FWHM}_{H\alpha}$ (3)	$L_{H\alpha}$ (4)	L_{bol} (5)	VP (6)	L_{bol}/L_{Edd} (7)	σ_* (8)
J004730.33+154149.4	0.0315	3460	40.1	42.7	6.05	-2.20	134
J005847.49-010549.6	0.0465	5090	40.6	43.1	6.59	-2.37	128
J010606.92+002025.1	0.0436	2880	40.1	42.7	5.87	-2.05	73
J013402.54-094626.9	0.0408	4530	41.1	43.6	6.74	-2.04	143
J015612.53+145423.9	0.0269	1930	40.5	43.0	5.70	-1.53	98
J030834.31+003303.3	0.0308	3120	40.4	43.0	6.10	-1.99	168
J031142.21+000853.3	0.0370	12990	40.5	43.1	7.42	-3.22	128
J032525.35-060837.9	0.0345	2400	41.4	43.8	6.31	-1.35	145
J033957.86-061215.1	0.0498	4520	40.5	43.0	6.44	-2.31	136
J074507.25+460420.6	0.0313	6120	40.5	43.0	6.74	-2.56	158
J075151.88+494851.5	0.0244	2740	40.4	43.0	5.98	-1.87	113
J075217.05+254008.7	0.0454	2960	40.2	42.8	5.95	-2.02	145
J075643.72+445124.1	0.0498	3540	40.6	43.1	6.29	-2.03	108
J075828.11+374711.8	0.0408	2710	40.8	43.3	6.13	-1.72	263
J080421.30+100610.9	0.0342	3530	40.6	43.1	6.29	-2.02	134
J081726.41+101210.1	0.0457	5640	40.7	43.2	6.75	-2.41	143
J082004.39+562320.6	0.0444	7930	40.6	43.1	7.00	-2.76	113
J082351.90+421319.4	0.0376	1980	40.3	42.9	5.62	-1.64	96
J082414.31+171955.0	0.0372	2010	40.7	43.2	5.84	-1.48	110
J082620.81+055727.8	0.0448	3420	40.5	43.1	6.23	-2.02	124
J084137.87+545506.5	0.0446	3200	41.0	43.5	6.39	-1.77	162
J084143.50+013149.8	0.0499	3640	40.6	43.1	6.31	-2.05	155
J090554.48+471045.5	0.0272	2550	40.3	42.8	5.84	-1.87	183
J091330.33+565128.4	0.0410	2050	40.3	42.8	5.64	-1.68	107
J091424.75+115625.5	0.0312	1350	40.0	42.6	5.16	-1.40	74
J091708.26+292215.6	0.0353	3390	40.2	42.8	6.08	-2.14	145
J092313.31+565622.2	0.0494	2810	40.5	43.0	6.03	-1.86	172
J092528.24+233630.9	0.0330	4550	40.6	43.1	6.49	-2.27	136
J093106.75+490447.1	0.0339	1980	40.4	43.0	5.68	-1.59	147
J093551.60+612111.3	0.0393	2260	40.9	43.3	6.00	-1.53	189
J093917.25+363343.8	0.0197	4020	40.3	42.9	6.27	-2.26	151
J094319.15+361452.1	0.0221	2650	40.3	42.9	5.91	-1.88	175
J094830.01+553822.6	0.0452	2100	40.5	43.1	5.79	-1.58	100
J094931.37+343819.5	0.0388	2260	40.6	43.1	5.89	-1.62	76
J095009.35+333409.5	0.0271	5000	40.2	42.8	6.41	-2.51	137
J095437.22+063719.5	0.0410	6960	41.1	43.6	7.14	-2.42	181
J095742.84+403315.9	0.0452	1820	40.3	42.9	5.57	-1.54	105
J095824.97+103402.4	0.0417	4850	40.1	42.7	6.36	-2.50	108
J100207.04+030327.6	0.0232	4580	40.8	43.3	6.61	-2.18	119
J101439.55-004951.2	0.0491	3120	40.6	43.1	6.16	-1.93	200
J101640.57+025125.2	0.0483	4370	40.1	42.7	6.24	-2.43	120
J101833.47+141241.1	0.0323	3460	40.5	43.0	6.22	-2.05	135
J101846.09+345001.6	0.0349	1650	40.6	43.2	5.62	-1.33	77
J104243.85+314121.8	0.0345	3650	40.0	42.6	6.05	-2.29	74
J104250.27+254616.3	0.0299	3360	41.0	43.5	6.41	-1.83	105
J104546.94+371240.7	0.0241	3040	39.6	42.3	5.69	-2.30	135
J104809.69+565459.4	0.0463	3790	40.5	43.0	6.29	-2.15	124
J104930.92+225752.3	0.0327	2300	40.5	43.1	5.87	-1.67	163
J105214.95+300328.3	0.0345	1940	40.5	43.1	5.71	-1.52	136
J105427.88+330943.4	0.0433	1960	40.8	43.3	5.84	-1.43	147
J105756.81+165434.4	0.0301	6250	40.4	42.9	6.69	-2.63	119
J105833.33+461604.8	0.0399	3500	40.7	43.2	6.32	-1.98	142
J110501.98+594103.5	0.0338	2530	41.0	43.5	6.18	-1.56	137
J111106.73+073459.8	0.0479	4690	40.6	43.1	6.52	-2.30	186
J111117.95+113315.8	0.0381	5880	40.9	43.4	6.86	-2.38	162
J111258.29+215434.0	0.0296	5210	40.3	42.9	6.51	-2.49	121
J111349.74+093510.7	0.0292	3940	41.2	43.6	6.65	-1.89	210
J111653.41+275822.8	0.0347	3680	40.5	43.0	6.27	-2.11	104
J111926.22+031205.7	0.0236	1960	39.7	42.3	5.34	-1.87	82
J112008.68+341845.8	0.0368	2540	40.3	42.9	5.86	-1.85	102

Table 1
continued

AGN (1)	z (2)	$\text{FWHM}_{H\alpha}$ (3)	$L_{H\alpha}$ (4)	L_{bol} (5)	VP (6)	L_{bol}/L_{Edd} (7)	σ_* (8)
J112011.14+340858.9	0.0352	2410	40.1	42.7	5.71	-1.89	71
J112135.17+042647.2	0.0470	1780	40.4	43.0	5.59	-1.49	100
J112637.73+513423.0	0.0265	1760	40.0	42.6	5.39	-1.64	93
J112726.64+264051.5	0.0329	4860	40.4	42.9	6.46	-2.42	129
J113355.93+670107.0	0.0397	6130	40.9	43.4	6.92	-2.40	156
J113409.01+491516.3	0.0373	2410	40.1	42.7	5.69	-1.91	70
J113543.71+490959.8	0.0353	2450	39.9	42.5	5.62	-2.00	105
J114223.58+153340.9	0.0444	1940	40.5	43.0	5.69	-1.55	82
J114530.25+094344.7	0.0214	3080	40.4	42.9	6.05	-2.00	159
J114612.17+202329.9	0.0233	5190	40.4	43.0	6.55	-2.45	195
J114840.42-001710.3	0.0474	3210	40.5	43.0	6.15	-1.98	208
J115246.29+232833.6	0.0220	5580	40.6	43.1	6.68	-2.45	169
J115623.23+195932.1	0.0409	3040	40.4	43.0	6.08	-1.96	136
J120144.91+201941.9	0.0234	1940	40.3	42.8	5.59	-1.63	123
J120234.39+544500.7	0.0499	4050	40.6	43.1	6.40	-2.16	93
J120443.31+311038.2	0.0249	4270	40.9	43.4	6.61	-2.06	127
J120704.75+090647.9	0.0344	6150	41.1	43.5	7.00	-2.33	168
J120908.80+440011.4	0.0376	2030	40.6	43.2	5.81	-1.52	143
J124054.96+080323.1	0.0477	1620	40.6	43.2	5.61	-1.32	97
J124240.45+092851.8	0.0240	2330	39.9	42.6	5.61	-1.92	76
J124610.76+275615.9	0.0231	4840	40.5	43.0	6.50	-2.37	123
J124954.76+503453.9	0.0469	2490	40.4	42.9	5.87	-1.80	133
J125258.13+090157.2	0.0400	3770	40.5	43.0	6.30	-2.13	175
J125552.36+103055.2	0.0484	4400	40.9	43.4	6.62	-2.11	130
J130340.81+534323.6	0.0276	1670	40.0	42.6	5.32	-1.62	136
J130342.82+324824.5	0.0367	1820	40.1	42.7	5.46	-1.64	74
J130422.19+361543.1	0.0443	1850	41.3	43.7	6.01	-1.19	137
J130620.97+531823.1	0.0237	8830	40.8	43.3	7.22	-2.75	141
J130705.01+024337.1	0.0477	4570	40.4	43.0	6.44	-2.32	147
J130737.68+433117.7	0.0353	3420	40.6	43.1	6.27	-1.99	83
J132209.96+331005.6	0.0373	1490	40.0	42.6	5.23	-1.51	78
J132336.84+062424.3	0.0394	2590	40.4	43.0	5.92	-1.83	85
J133204.81+170256.2	0.0215	4140	40.7	43.2	6.49	-2.12	152
J134244.42+350346.4	0.0243	2300	40.1	42.7	5.69	-1.83	87
J134249.94+294546.4	0.0431	2900	40.8	43.3	6.21	-1.76	170
J135419.95+325547.7	0.0261	4220	40.8	43.3	6.55	-2.09	177
J135747.63+072346.5	0.0236	3720	40.1	42.7	6.09	-2.29	100
J140543.16+251352.9	0.0298	6230	40.7	43.2	6.85	-2.48	139
J140718.28+125313.9	0.0274	4980	40.2	42.8	6.40	-2.50	139
J140804.00+071939.4	0.0239	1890	40.4	42.9	5.62	-1.56	82
J141057.23+252950.0	0.0310	2400	40.5	43.1	5.91	-1.71	175
J141809.22+073352.3	0.0247	4500	40.2	42.8	6.31	-2.42	299
J142042.91+262503.2	0.0379	1900	40.8	43.3	5.83	-1.38	130
J142255.33+325102.3	0.0342	4060	40.8	43.3	6.48	-2.09	140
J142307.51+283542.3	0.0293	2810	40.6	43.1	6.07	-1.83	130
J142704.54+355409.5	0.0290	5930	40.9	43.3	6.86	-2.39	179
J143318.47+344404.4	0.0343	3180	40.5	43.0	6.13	-1.99	202
J143727.85+254556.0	0.0328	1200	39.6	42.3	4.86	-1.47	136
J144331.28+492335.1	0.0302	6920	40.6	43.2	6.91	-2.61	137
J144629.99+500130.7	0.0427	6110	41.0	43.5	6.97	-2.35	132
J144837.03+514331.0	0.0364	2170	40.3	42.8	5.69	-1.73	71
J145048.68+200301.4	0.0437	5170	40.4	43.0	6.56	-2.43	154
J150214.29+182928.7	0.0477	2090	40.5	43.1	5.79	-1.58	81
J150511.42-020831.0	0.0372	5950	40.3	42.9	6.63	-2.60	138
J150653.38+125131.2	0.0216	1840	39.7	42.4	5.30	-1.79	106
J150656.41+125048.6	0.0224	2980	40.2	42.7	5.93	-2.06	217
J151512.25+152412.3	0.0457	1540	40.7	43.2	5.60	-1.23	98
J151907.55+260750.6	0.0447	2520	40.5	43.0	5.92	-1.78	117
J154357.33+283126.4	0.0323	1580	40.6	43.1	5.57	-1.30	110
J154744.14+412408.2	0.0326	1900	40.7	43.2	5.77	-1.44	89

Table 1
continued

AGN (1)	z (2)	FWHM $_{H\alpha}$ (3)	$L_{H\alpha}$ (4)	L_{bol} (5)	VP (6)	L_{bol}/L_{Edd} (7)	σ_* (8)
J155926.11+521235.3	0.0423	4380	40.9	43.4	6.64	-2.08	134
J160154.01+315331.3	0.0450	3240	40.9	43.4	6.35	-1.83	178
J160417.30+042135.7	0.0465	3660	40.3	42.8	6.16	-2.20	124
J160445.00+444316.9	0.0433	2460	40.4	42.9	5.86	-1.79	107
J160505.15+452634.8	0.0434	5870	41.1	43.6	6.98	-2.27	178
J160652.16+275539.1	0.0463	3250	41.1	43.5	6.43	-1.76	128
J160746.71+253214.9	0.0406	1440	40.2	42.8	5.30	-1.38	96
J161243.05+002247.9	0.0445	9230	40.8	43.3	7.22	-2.82	189
J161630.67+354228.9	0.0278	5730	40.5	43.0	6.68	-2.50	151
J162131.63+245952.4	0.0378	3250	40.5	43.0	6.15	-2.01	110
J162938.37+384139.2	0.0356	1600	39.9	42.5	5.25	-1.61	71
J163453.66+231242.6	0.0387	3810	41.0	43.5	6.55	-1.92	144
J164107.63+224924.8	0.0339	2810	40.6	43.1	6.09	-1.82	89
J164520.61+424528.0	0.0494	5050	40.6	43.1	6.60	-2.35	98
J171518.57+573931.6	0.0281	4340	40.1	42.7	6.25	-2.40	131
J173159.21+595817.9	0.0292	4440	40.1	42.7	6.28	-2.42	153
J173809.30+584253.6	0.0288	6130	40.6	43.1	6.78	-2.52	125
J204745.25-052515.6	0.0458	3200	40.9	43.4	6.35	-1.81	156
J210917.64+001619.1	0.0500	13500	41.1	43.5	7.70	-3.04	169
J230920.26+004523.3	0.0323	5690	41.0	43.5	6.92	-2.28	142
J232337.44+133908.1	0.0425	2850	40.4	43.0	6.01	-1.91	193
J232611.29+140148.1	0.0462	7190	40.4	43.0	6.85	-2.73	143

NOTES. Column 1: Object name. Column 2: Redshift. Column 3: FWHM velocity of the broad component of the $H\alpha$ emission line in km s^{-1} . Column 4: Luminosity of the broad component of the $H\alpha$ emission line in log scale (erg s^{-1}). Column 5: Bolometric luminosity in log scale (erg s^{-1}). Column 6: Virial Product in log scale (M_\odot). Column 7: Eddington ratio in log scale. Column 8: Stellar velocity dispersion in km s^{-1} adopted from the SDSS catalogue.

this should be considered as a lower limit because we conservatively identified the broad $H\alpha$ component by excluding AGNs that require a broad component with relatively small width. If we extrapolate the fraction of the misclassified type 1 AGNs, 3.5%, to higher redshift, it is expected that a large number of AGNs could be misclassified as type 2 AGNs in the SDSS DR7 catalog. The discovery of the missing type 1 AGN population will shed light on understanding the low-mass, low-luminosity AGNs and studying AGN population and their properties.

The newly identified type 1 AGN sample has a mean black hole mass $\log(M_{BH}/M_\odot) = 6.94 \pm 0.51$ based on the most recent single-epoch black hole mass calibrator – although the precise black hole mass values depend on the virial factor. The mean broad $H\alpha$ luminosity of the sample is $\log(L_{H\alpha}/(\text{erg s}^{-1})) = 40.50 \pm 0.35$, and the mean Eddington ratio is $\log L_{bol}/L_{Edd} = -2.00 \pm 0.40$. The low Eddington ratios of the sample imply that the AGN continuum is too weak to change the host galaxy color, which is consistent with the relatively red color of the targets shown in the SDSS images.

We investigated the velocity offset of each emission line with respect to the systemic velocity measured from stellar absorption lines. We find that the O III lines show relatively large velocity offsets while the velocity offsets of the $H\alpha$ lines are weaker than for O III, indicating that the O III-emitting gas is influenced by outflows more strongly. The velocity dispersions of the N II lines and the O III core components are consistent

with each other and with stellar velocity dispersions, albeit with significant scatter, suggesting that the kinematics of the gas in the NLR is mainly governed by the large scale gravitational potential (i.e., the galaxy bulge), while outflow/inflow motions can vary the velocity dispersion of narrow emission lines. The kinematic properties of the ionized gas of the sample are similar to those of the general type 1 AGN population, supporting the idea that these objects are simply misclassified type 1 AGNs.

ACKNOWLEDGMENTS

This work was supported by the National Research Foundation of Korea (NRF) grant funded by the Korean government (MEST; No. 2012-R1A2A2A01006087). J.H.W. acknowledges the support by the Korea Astronomy and Space Science Institute (KASI) grant funded by the Korea government (MEST). by the Korea government (No. 2012-006087). J.G.K. acknowledges the support by the 2012 R&E Program of Gyeonggi Science High School for the Gifted (GSHS).

REFERENCES

- Abazajian, K. N., et al. 2009, The Seventh Data Release of the Sloan Digital Sky Survey, *ApJS*, 182, 543
 Bae, H.-J. & Woo, J.-H. 2014, A Census of Gas Outflows in Type 2 Active Galactic Nuclei *ApJ*, 795, 30
 Baldwin, J. A., Phillips, M. M., & Terlevich, R. 1981, *Classi-*

- fication Parameters for the Emission-Line Spectra of Extragalactic Objects, *PASP*, 93, 5
- Blandford, R. D., & McKee, C. F. 1982, Reverberation Mapping of the Emission Line Regions of Seyfert Galaxies and Quasars, *ApJ*, 255, 419
- Bellovary, J., Holley-Bockelmann, K., Gültekin, K., et al. 2014, Effects of Inclination on Measuring Velocity Dispersion and Implications for Black Holes, *ApJ*, in press (arXiv:1405.0286)
- Bentz, M. C., Denney, K. D., Grier, C. J., Barth, A. J., Peterson, B. M., Vestergaard M., Bennert, V. N., Canalizo, G., De Rosa, G., Filippenko, A. V., Gates, E. L., Greene, J. E., Li, W., Malkan, M. A., Pogge, R. W., Stern, D., Treu, T., & Woo, J.-H. 2013, The Low-Luminosity End of the Radius-Luminosity Relationship for Active Galactic Nuclei, *ApJ*, 767, 149
- Boroson, T. 2005, Blueshifted [O III] Emission: Indications of a Dynamic Narrow-Line Region, *AJ*, 130, 381
- Cappellari, M., & Emsellem, E. 2004, Parametric Recovery of Line-of-Sight Velocity Distributions from Absorption-Line Spectra of Galaxies via Penalized Likelihood, *PASP*, 116, 138
- Choi, Y.-Y., Han, D.-H., & Kim, S. S. 2010, Korea Institute for Advanced Study Value-Added Galaxy Catalog, *JKAS*, 43, 191
- Crenshaw, D. M., Schmitt, H. R., Kraemer, S. B., Mushotzky, R. F., & Dunn, J. P. 2010, Radial Velocity Offsets Due to Mass Outflows and Extinction in Active Galactic Nuclei, *ApJ*, 708, 419
- Glikman, E., Helfand, D. J., White, R. L., et al. 2007, The FIRST-2MASS Red Quasar Survey, *ApJ*, 667, 673
- Glikman, E., Urrutia, T., Lacy, M., et al. 2013, Dust Reddened Quasars in FIRST and UKIDSS: Beyond the Tip of the Iceberg, *ApJ*, 778, 127
- Greene, J. E., & Ho, L. C. 2004, Active Galactic Nuclei with Candidate Intermediate-Mass Black Holes, *ApJ*, 610, 722
- Greene, J. E., & Ho, L. C. 2005, Estimating Black Hole Masses in Active Galaxies Using the $H\alpha$ Emission Line, *ApJ*, 630, 122
- Greene, J. E., & Ho, L. C. 2007, A New Sample of Low-Mass Black Holes in Active Galaxies, *ApJ*, 670, 92
- Haring, N., Rix, H. W. 2004, On the Black Hole Mass-Bulge Mass Relation, *ApJ*, 604, L89
- Heckman, T., & Best, P. 2014, The Coevolution of Galaxies and Supermassive Black Holes: Insights from Surveys of the Contemporary Universe, *ARAA*, 52, 589
- Hornschemeier, A. E., Heckman, T. M., Ptak, A. F., Tremonti, C. A., & Colbert, E. J. M. 2005, Chandra-SDSS Normal and Star-Forming Galaxies. I. X-Ray Source Properties of Galaxies Detected by the Chandra X-Ray Observatory in SDSS DR2, *AJ*, 129, 86
- Kang, W.-R., Woo, J.-H., Schulze, A., et al. 2013, Calibrating Stellar Velocity Dispersions Based on Spatially Resolved H-band Spectra for Improving the $M_{BH} - \sigma_*$ Relation *ApJ*, 767, 26
- Kaspi, S., Smith, P. S., Netzer, H., Maoz, D., Jannuzi, B. T., & Giveon, U. 2000, Reverberation Measurements for 17 Quasars and the Size-Mass-Luminosity Relations in Active Galactic Nuclei, *ApJ*, 533, 631
- Kelly, B. C., & Shen, Y. 2013, The Demographics of Broad-line Quasars in the Mass-Luminosity Plane. II. Black Hole Mass and Eddington Ratio Functions, *ApJ*, 764, 45
- Kewley, L. J., Groves, B., Kauffmann, G., & Heckman, T. 2006, The Host Galaxies and Classification of Active Galactic Nuclei, *MNRAS*, 372, 961
- Komossa, S., Xu, D., Zhou, H., Storchi-Bergmann, T., & Binette, L. 2008, On the Nature of Seyfert Galaxies with High [O III] 5007 Blueshifts, *ApJ*, 680, 926
- Koratkar A. P., & Gaskell, C. M. 1991, Radius-Luminosity and Mass-Luminosity Relationship for Active Galactic Nuclei, *ApJ*, 370, L61
- Kormendy, J., & Ho, L. C. 2013, Coevolution (Or Not) of Supermassive Black Holes and Host Galaxies, *ARAA*, 51, 511
- Land, K., Slosar, A., Lintott, C., Andreescu, D., Bamford, S., Murray, P., Nichol, R., Raddick, M. J., Schawinski, K., Szalay, A., Thomas, D., & Vandenberg, J. 2008, Galaxy Zoo: the large-scale spin statistics of spiral galaxies in the Sloan Digital Sky Survey, *MNRAS*, 388, 1686
- Lintott, C. J., Schawinski, K., Slosar, A., Land, K., Bamford, S., Thomas, D., Raddick, M. J., Nichol, R. C., Szalay, A., Andreescu, D., Murray, P., & Vandenberg, J. 2008, Galaxy Zoo: morphologies derived from visual inspection of galaxies from the Sloan Digital Sky Survey, *MNRAS*, 389, 1179
- Lintott, C. J., Schawinski, K., Bamford, S., Slosar, A., Land, K., Thomas, D., Edmondson, E., Masters, K., Nichol, R. C., Raddick, M. J., Szalay, A., Andreescu, D., Murray, P., & Vandenberg, J. 2011, Galaxy Zoo 1: data release of morphological classifications for nearly 900 000 galaxies, *MNRAS*, 410, 166
- Markwardt, C. B. 2009, Non-Linear Least-Squares Fitting in IDL with MPFIT, *ASPC*, 411, 251
- McConnell, N. J., & Ma, C.-P. 2013, Revisiting the Scaling Relations of Black Hole Masses and Host Galaxy Properties, *ApJ*, 764, 14
- Nelson, C. H., & Whittle, M. 1995, Stellar and Gaseous Kinematics of Seyfert Galaxies. I. Spectroscopic Data, *ApJS*, 99, 67
- Netzer, H. 2009, Accretion and star formation rates in low-redshift type II active galactic nuclei, *MNRAS*, 399, 1907
- Oh, K., Sarzi, M., Schawinski, K., & Yi, S. K. 2011, Improved and Quality-assessed Emission and Absorption Line Measurements in Sloan Digital Sky Survey Galaxies, *ApJS*, 195, 13
- Onken, C. A., Ferrarese, L., Merritt, D., Peterson, B. M., Pogge, R. W., Vestergaard, M., & Wandel, A. 2004, Supermassive Black Holes in Active Galactic Nuclei. II. Calibration of the Black Hole Mass-Velocity Dispersion Relationship for Active Galactic Nuclei, *ApJ*, 615, 645
- Park, D., Woo, J.-H., Treu, T., Barth, A. J., Bentz, M. C., Bennert, V. N., Canalizo, G., Filippenko, A. V., Gates, E., Greene, J. E., Malkan, M. A., & Walsh, J. 2012, The Lick AGN Monitoring Project: Recalibrating Single-epoch Virial Black Hole Mass Estimates, *ApJ*, 747, 30
- Reines, A. E., Greene, J. E., & Geha, M. 2013, Dwarf Galaxies with Optical Signatures of Active Massive Black Holes, *ApJ*, 775, 116
- Richards, G. T., Lacy, M., Storrie-Lombardi, L. J., Hall, P. B., Gallagher, S. C., Hines, D. C., Fan, X., Papovich, C., Vanden Berk, D. E., Trammell, G. B., Schneider, D. P., Vestergaard, M., York, D. G., Jester, S., Anderson, S. F., Budavári, T., & Szalay, A. S. 2006, Spectral Energy Distributions and Multiwavelength Selection of Type 1 QUASARS, *ApJS*, 166, 470
- Schawinski, K., Urry, C. M., Virani, S., Coppi, P., Bamford, S. P., Treister, E., Lintott, C. J., Sarzi, M., Keel, W. C., Kaviraj, S., Cardamone, C. N., Masters, K. L., Ross, N. P., Andreescu, D., Murray, P., Nichol, R. C., Raddick, M. J., Slosar, A., Szalay, A. S., Thomas, D., & Vandenberg,

- J. 2010, Galaxy Zoo: The Fundamentally Different Co-Evolution of Supermassive Black Holes and Their Early- and Late-Type Host Galaxies, *ApJ*, 711, 284
- Shen, J., Vanden Berk, D. E., Schneider, D. P., & Hall, P. B. 2008, The Black Hole-Bulge Relationship in Luminous Broad-Line Active Galactic Nuclei and Host Galaxies, *ApJ*, 135, 928
- Stern, J., & Laor, A. 2012, Type I AGN at low z . I. Emission properties, *MNRAS*, 423, 600
- Seyfert, C. K. 1943, Nuclear Emission in Spiral Nebulae, *ApJ*, 97, 28
- Verolme, E. K., Cappellari M., Copin, Y., van der Marel, R. P., Bacon, R., Bureau, M., Davies, R. L., Miller, B. M., & de Zeeuw, P. T. 2002, A SAURON Study of M32: Measuring the Intrinsic Flattening and the Central Black Hole Mass, *MNRAS*, 355, 517
- Woo, J.-H., Treu, T., Malkan, M. A., & Blandford, R. D. 2006, Cosmic Evolution of Black Holes and Spheroids. I. The $M_{BH} - \sigma_*$ Relation at $z = 0.36$, *ApJ*, 645, 900
- Woo, J.-H., Treu, T., Barth, A. J., Wright, S. A., Walsh, J. L., Bentz, M. C., Martini, P., Bennert, V. N., Canalizo, G., Filippenko, A. V., Gates, E., Greene, J., Li, W., Malkan, M. A., Stern, D., & Minezaki, T. 2010, The LICK AGN Monitoring Project: The $M_{BH} - \sigma_*$ Relation for Reverberation-Mapped Active Galaxies, *ApJ*, 716, 269
- Woo, J.-H., & Urry, C. M. 2002, Active Galactic Nucleus Black Hole Masses and Bolometric Luminosities, *ApJ*, 579, 530
- Woo, J.-H., Schulze, A., Park, D., Kang, W.-R., Kim, S. C., & Riechers, D. A. 2013, Do Quiescent and Active Galaxies Have Different $M_{BH} - \sigma_*$ Relations?, *ApJ*, 772, 49
- Wyithe, J. S. B., & Loeb, J. 2002, A Physical Model for the Luminosity Function of High-Redshift Quasars, *ApJ*, 581, 886
- Xiao, T., Barth, A. J., Greene, J. E., Ho, L. C., Bentz, M. C., Ludwig, R. R., & Jiang, Y. 2011, Exploring the Low-Mass End of the $M_{BH} - \sigma_*$ Relation with Active Galaxies, *ApJ*, 739, 28